Vol. 37, No. 4 (2015) 400-412

Tribology in Industry

www.tribology.fink.rs

RESEARCH

Development of a Constitutive Friction Law based on the Frictional Interaction of Rough Surfaces

F. Beyer [a], F. Hauer [a], K. Willner [a]

[a] *Chair of Applied Mechanics, Friedrich-Alexander-Universität Erlangen-Nürnberg, Egerlandstr. 5, 91058 Erlangen, Germany.*

Keywords:

Half-space
Elasto-plastic contact
Simulation
Constitutive friction law
Sheet-bulk metal forming

Corresponding author:

F. Beyer
Chair of Applied Mechanics,
Friedrich-Alexander-Universität
Erlangen-Nürnberg, Egerlandstr. 5,
91058 Erlangen
E-mail: florian.beyer@ltm.uni-erlangen.de

A B S T R A C T

Friction has a considerable impact in metal forming. This is in particular true for sheet-bulk metal-forming (SBMF) in which local highly varying contact loads occur. A constitutive friction law suited to the needs of SBMF is necessary, if numerical investigations in SBMF are performed. The identification of the friction due to adhesion and ploughing is carried out with an elasto-plastic half-space model. The normal contact is verified for a broad range of normal loads. In addition, the model is used for the characterization of the occurring shear stress. Ploughing is determined by the work which is necessary to plastically deform the surface asperities of the new area that gets into contact during sliding. Furthermore, the surface patches of common half-space models are aligned orthogonally to the direction in which the surfaces approach when normal contact occurs. For a better reflection of the original surfaces, the element patches become inclined. This leads to a geometric share of lateral forces which also contribute to friction. Based on these effects, a friction law is derived which is able to predict the contact conditions especially for SBMF.

1. INTRODUCTION

Friction exerts a great influence on metal forming processes both in economic and technical terms. Usually, friction appears with an unintended loss of energy and with negative impact on the material. For example, friction causes energy dissipation due to heat generation and the occurring stresses due to friction lead to microscopic cracks which wear out the surface of a worktool [1]. These effects permanently decrease the functionality and availability of either the desired product or the worktool of the forming process.

Furthermore, if process factors like strain, stresses or the force path have to be evaluated numerically or analytically, a mathematical connection is necessary which describes the contact condition between the contacting partners, i.e. the contact between the workpiece and the worktool.

However, the choice of the appropriate friction law depends on the considered metal forming process which can be broadly classified into sheet metal forming and bulk metal forming. Sheet metal forming incorporates low to moderate contact loads. For this case, Coulomb's

friction law is a valid assumption. Further advanced friction models for sheet metal forming have been proposed by Westeneng [2] for deep drawing which is based on a contact model assuming plastic deformation of the workpiece deformation, by Hol [3] which includes hydrodynamic friction with focus on the load-carrying capacity of the lubricant or by Zöller [4] which is a solely pressure dependent friction model.

If the contact loads are high, which is the case in bulk forming processes, a friction model depending on the yield stress is more suitable. For example, Tresca's friction law is a good assumption since the resulting friction stress is expressed in dependency on the shear yield stress. The choice of a suitable friction law complicates if the complex properties of both sheet metal forming and bulk forming are combined in one process. An example for such a combination is sheet-bulk metal forming (SBMF) in which half-finished products made of sheet metal are deformed by bulk forming processes [5]. The importance of friction in SBMF was shown in terms of mould filling as mould filling is significantly altered by the frictional state [6]. It seems to be evident, that a friction law which is especially suited for the unique contact conditions in SBMF is necessary.

The findings of Shaw [7] provide a promising start since the friction model combines Coulomb's friction model with Tresca's law. Furthermore, for deep drawing it was shown that plastic smoothing of rough surface changes the friction condition [8] for multi-stage processes. As SBMF can also be performed incrementally, this effect has to be taken into account, too. The numerical study of friction requires a fine discretization of the contact area due to the multi-scale character of rough surfaces. Hence, a half-space approximation is preferred as it only depends on the two-dimensional surface boundary [9] which consumes less computing capacity than FEM with its three-dimensional volume discretization for the same surface resolution. Kalker was one of the first who presented a half-space model [10]. The model is based on the minimum total complementary potential energy principle for the solution of elastic problems and it is extendable to elasto-plastic contact by limiting the local bearable load of the surface, as derived by Hencky [11] and experimentally validated by Bowden and Tabor [12].

Kim et al. [13] used an elasto-plastic model for the investigation of non-Gaussian rough surfaces, Tian and Bhushan [14] modelled normal contact between a rough surface and a rigid sphere and Willner [15] took into account fractal surfaces. Furthermore, Polonsky and Keer [16] used a multi-mesh and a conjugate gradient method for the computation of the half-space model which was compared by Allwood [17] in terms of performance with other well-established solution methods in the framework of half-space models. There is also the possibility to model three-dimensional plastic deformation based on volume discretization and the reciprocal stress theorem as derived by Jacq et al. [18] which was improved by Wang and Keer [19] in terms of the residual displacement increment and by Nèlias et al. [20] in terms of an improved plasticity loop.

Additionally, research regarding tangential contact with half-space models is vastly spread. Kalker developed a contact model for both normal and tangential contact which was used to simulate rolling contact [21]. Vàradi et al. [22] applied the half-space on sliding contact of metallic surfaces, in which an elastic contact algorithm was used focused on thermal interaction. Willner [23] regarded coupling between normal and tangential motion and investigated therewith rough contact. A similar approach was presented by Chen and Wang [24] who focused on spherical contact of rough surfaces. Finally, three-dimensional models based on volume discretization are also expandable to tangential contact as proposed by Fulleringer and Nèlias [25] and applied for sliding and rolling contact by Boucly et al. [26].

However, the half-space model which is used for the later studies of the frictional interaction between two rough surfaces is based on a simplified elasto-plastic half-space model since it comes with less numerical effort and thus is faster. The model which is described in Sec. 2 is able to evaluate normal and tangential contact. It is used to research friction due to adhesion and ploughing as they are the main contributions in metallic contact to friction [12]. In Sec. 3.1 it is shown that the half-space model successfully predicts the elasto-plastic contact, although it

incorporates only simplified plasticity. The normal contact is used to analyse the evolution of the real contact area in dependency on the applied contact since the real contact area is a measure for the transferable adhesive forces. Sec. 3.2 extends the half-space model in order to investigate a friction share which we call geometric friction. Common half-space models align each surface patch perpendicular to the direction in which the contact partners approach for normal contact. In this section, the surface patches become inclined since sloped surface elements approximate the actual surface more precisely. In Sec. 3.3 sliding contact is investigated for the determination of the frictional share due to ploughing. Finally, Sec. 4 describes the proposed friction law which is suited to the needs of SBMF.

2. NUMERICAL MODEL

2.1 Normal Contact

The half-space model for normal contact is a linear system of equations which are based on the analytic Boussinesq potentials [27]. The dependency of the normal load p at (x', y') in the domain of contact Ω on the normal displacement u_z at (x, y) is given with:

$$u_z(x,y)=\frac{1-\nu^2}{\pi E}\iint_{\Omega}\frac{p(x',y')\mathrm{d}x'\mathrm{d}y'}{\sqrt{(x-x')^2+(y-y')^2}}, \quad (1)$$

where E is Young's modulus and ν is Poisson's ratio. Since the materials of both partners are elastic, $E/(1-\nu^2)$ is replaced with the composite elastic modulus [28] E^* which is obtained as:

$$\frac{1}{E^*}=\frac{1-\nu_1^2}{E_1}+\frac{1-\nu_2^2}{E_2}, \quad (2)$$

where the indices refer to each contact partner. For rough contact Tian and Bhushan developed a model [14] that is able to calculate the interdependency between surface pressure and normal surface displacement. The approach, which is also used here, relies on the minimization of the complementary energy which in turn is based on a variational principle.

The surfaces of both contact partners are discretized into $N_x \times N_y = M$ rectangular elements with size $2a \times 2b$ as shown in Fig. 1.

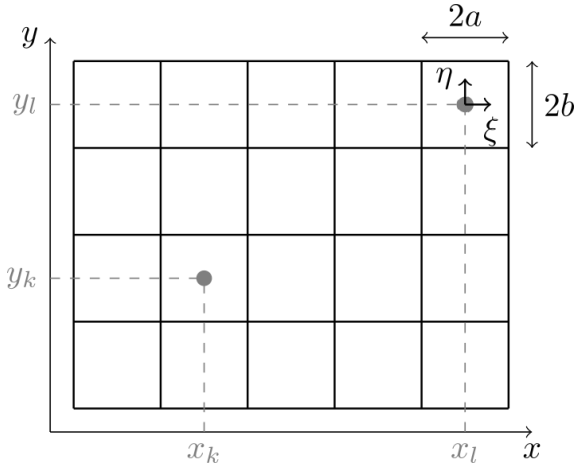

Fig. 1. Top view of discretized surface.

Since the system is linear, the superposition of the surface displacement due to all elements l that are in contact yields the normal displacement of an arbitrary element k. The corresponding field problem is given by:

$$u_{z,k}=\sum_{l=1}^{M}C_{kl}^{zz}p_l. \quad (3)$$

The influence coefficient matrix C_{kl}^{zz} is obtained with the Boussinesq potential as:

$$C_{kl}^{zz}=\frac{1}{\pi E^*}\int_{-a}^{a}\int_{-b}^{b}\frac{\mathrm{d}\xi\mathrm{d}\eta}{\rho}, \quad (4)$$

with

$$\rho=\sqrt{(x_k-x_l-\xi)^2+(y_k-y_l-\eta)^2}. \quad (5)$$

Its evaluation is given by Love [29]. As no tension stress occurs in normal direction, the condition:

$$p_l \geq 0 \quad l=1,...,M \quad (6)$$

has to be fulfilled. The local gap distance g_k between the surface patches is derived from Fig. 2 with:

$$g_k=h_{max}-h_k+u_{z,k}-u_0, \quad (7)$$

where h_{max} is the maximum height coordinate, h_k is the local height coordinate and u_0 is the global normal approach of the surfaces.

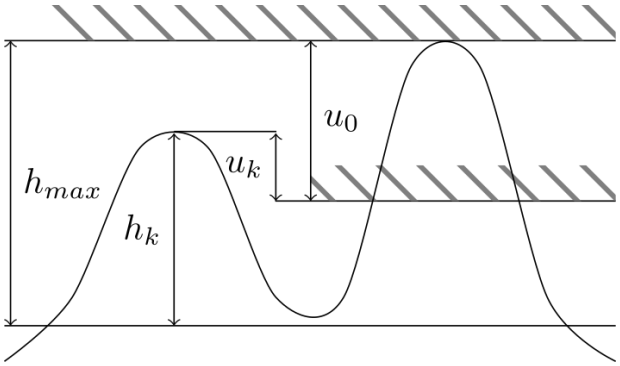

Fig. 2. Side view of contact approach.

The elastic problem itself is solved with an active set strategy in conjunction with the conjugate gradient method, as it is highly accurate and needs little memory compared to other solution methods [17]. Eq. (7) is solved for u_0 in such a way that the desired average contact load p_{mean} is reached at the whole surface.

Elasto-plastic contact is included by limiting the local contact load to an upper bound with:

$$p_l \le H \quad l = 1,...,M, \tag{8}$$

where H is the surface hardness. According to Bowden and Tabor [12] H depends on the yield stress σ_y of the weaker contact material with $H \approx 2.8 \cdot \sigma_y$. The local displacement $u_{z,k}$ is split into an elastic displacement $u_{z,k}^{el}$ and a plastic displacement $u_{z,k}^{pl}$. The latter is determined after obtaining the elastic solution. Contact elements with a normal load surpassing H are added to a '*plastic set*' [30] in which the normal load is set to H. A deformation field due to the plastic set is evaluated. Afterwards, the elastic problem is restarted with an altered gap function:

$$g_k = h_{max} - h_k + u_{z,k}^{pl} + u_{z,k}^{el} - u_0 \tag{9}$$

and solved for p_{mean} from which the load caused by the plastic set is subtracted. The plastic algorithm iteratively corrects $u_{z,k}^{pl}$ until the solution converges. Finally, for the sake of volume conservation, the volume reduced due to $u_{z,k}^{pl}$ is added evenly on the element patches that are not in contact based on the findings of Pullen and Williamson [31].

2.2 Uncoupled tangential contact

If, in addition to p, the in-plane surface tractions q_x and q_y are taken into account for x- and y-direction respectively, the normal contact model is expandable to determine fully coupled frictional contact. The relations between the tractions and displacements are given by

$$u_{x,k} = \sum_{l=1}^{M} \left(C_{kl}^{xx} q_{x,l} + C_{kl}^{xy} q_{y,l} + C_{kl}^{xz} p_l \right), \tag{10}$$

$$u_{y,k} = \sum_{l=1}^{M} \left(C_{kl}^{yx} q_{x,l} + C_{kl}^{yy} q_{y,l} + C_{kl}^{yz} p_l \right), \tag{11}$$

$$u_{z,k} = \sum_{l=1}^{M} \left(C_{kl}^{zx} q_{x,l} + C_{kl}^{zy} q_{y,l} + C_{kl}^{zz} p_l \right). \tag{12}$$

However, Willner [23] showed that the differences of the solutions between a coupled and an uncoupled contact model vanish, if the contact surfaces are rough and the material properties of the contact partners, i.e. E and ν, are identical. Therefore, an uncoupled approach is viable. Considering relative displacement between the contact partners only in x-direction the system of equations is simplified to:

$$u_{x,k} = \sum_{l=1}^{M} C_{kl}^{xx} q_{xl}, \tag{13}$$

$$u_{z,k} = \sum_{l=1}^{M} C_{kl}^{zz} p_l. \tag{14}$$

The flexibility matrix C_{kl}^{xx} is based on the Cerruti solution [32] which relates - similar to the Boussinesq solution - the displacement in x-direction $u_x(x,y)$ with the traction $q_x(x',y')$ with:

$$u_x(x,y) = \frac{1-\nu^2}{\pi E} \iint_{\Omega} \frac{q_x(x',y')\,\mathrm{d}x'\mathrm{d}y'}{\sqrt{(x-x')^2 + (y-y')^2}} + \frac{\nu(1+\nu)}{\pi E} \iint_{\Omega} \frac{q_x(x',y') \cdot (x-x')^2\,\mathrm{d}x'\mathrm{d}y'}{\sqrt{(x-x')^2 + (y-y')^2}}, \tag{15}$$

which in turn yields C_{kl}^{xx} as:

$$C_{kl}^{xx} = \frac{1}{\pi E^*} \int_{-a}^{a} \int_{-b}^{b} \frac{\mathrm{d}\xi\mathrm{d}\eta}{\rho} + \frac{1}{\pi E'} \int_{-a}^{a} \int_{-b}^{b} \frac{(x_k - x_l - \xi)^2\,\mathrm{d}\xi\mathrm{d}\eta}{\rho^3}, \tag{16}$$

with

$$\frac{1}{E'} = \frac{\nu_1(1+\nu_1)}{E_1} + \frac{\nu_2(1+\nu_2)}{E_2}. \tag{17}$$

The restrictions from Eq. (6) and Eq. (8) still apply. Furthermore, we limit the local traction $q_{x,l}$ with:

$$q_{x,l} \le m \cdot \frac{\sigma_y}{2} \quad l = 1,...,M \quad 0 \le m \le 1, \qquad (18)$$

which means that the upper bound of $q_{x,l}$ is limited by Tresca's law of friction where m is Tresca's friction coefficient.

The evaluation of the uncoupled tangential contact starts with the determination of the normal contact which solves Eq. (14) according to Sec. 2.1. That followed, Eq. (13) is solved by a Gauss-Seidel iteration for the unknown traction q_x similar to [23].

3. CONTACT SIMULATION

3.1 Normal contact

The first investigation focuses solely on normal contact and thus applies the model from Sec. 2.1. The model solves the surface approach of two contact partners in dependency on the mean pressure p_{mean}. As the normal approach is founded on asperity contact, it is possible to find local positions of the rough surface without contact. Therefore, the real contact area A_{real} is only a fraction of the apparent area A_0. The model evaluates the contact-dependent local pressure p, the average contact pressure p_{mean} and the real contact A_{real} which is later important for the deduction of the constitutive friction law.

The elasto-plastic deformable surface was measured from an electric discharge texture (EDT) on a 2mm thick sheet metal made of DC04. DC04 is a typical sheet metal material in SBMF and the EDT yields a characteristic surface roughness for SBMF. The elastic contact surface was measured from a stamp surface made of hardened steel (hardness ≈ 60HRC). The normal contact was performed with different loads which ranged from 100 MPa to 600 MPa in steps of 100 MPa. Each contact load was also experimentally performed on 5 samples. The surfaces before and after contact were measured with a Keyence VK-X105 laser microscope.

The numerical simulations were carried out with a square-shaped portion of the surfaces reaching a length of $L_x = L_y = 2.11$mm in x- and y-direction respectively. The surfaces were sampled down to $N_x \times N_y = 128 \times 128$ elements for a faster calculation. The material parameters as well as the centre-line average R_a and the root mean square roughness R_q of the simulated surfaces are given in Table 1. In order to bring the simulations and experiments into line, the surface hardness of the DC04 surface was set to $H = 800$ MPa in the half-space model. As the hardened steel of the stamp is much harder than DC04, the stamp surface was treated solely elastically.

Table 1. Material & surface parameters.

DC04	Hardened steel
$E_1 = 2.1 \cdot 10^{11} \frac{N}{m^2}$	$E_1 = E_2$
$\nu_1 = 0.3$	$\nu_2 = \nu_1$
$H = 8.0 \cdot 10^8 \frac{N}{m^2}$	
$R_a = 1.034\ \mu m$	$R_a = 0.102\ \mu m$
$R_q = 1.267\ \mu m$	$R_q = 0.160\ \mu m$

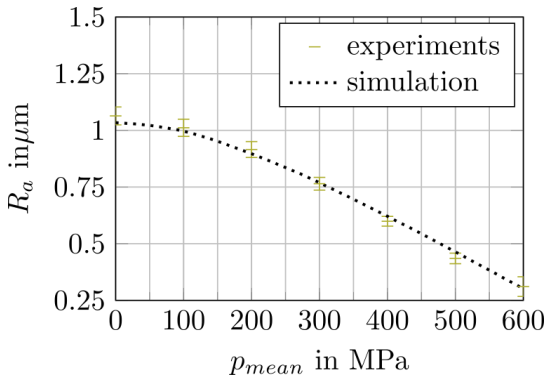

Fig. 3. R_a of elasto-plastic surface in dependency on p_{mean}.

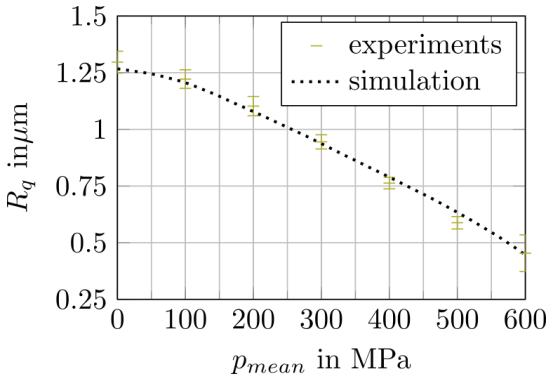

Fig. 4. R_q of elasto-plastic surface in dependency on p_{mean}

The change of the surface deformation of the elasto-plastic DC04 surface in dependency on the normal contact load is shown in Fig. 3 and Fig. 4 by means of R_a and R_q after the contact. The results of the simulations are compared with the mean values of the experiments which coincide very well.

3.2 Influence of inclined surface patches

Down-sampling and discretizing a surface comes with the effect that each part of the continuous surface area becomes represented by the mean height value of the corresponding area. Furthermore, for the half-space model each contact element is aligned into the normal direction of the normal contact approach. For example, Fig. 5 shows the discretized surface line which was originally represented in Fig. 2.

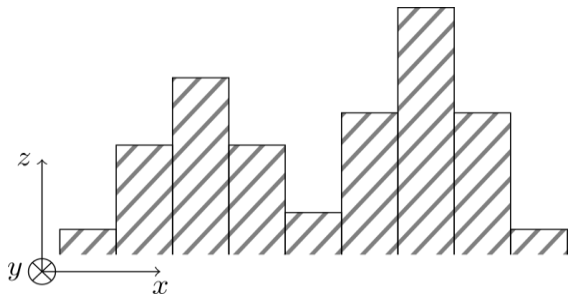

Fig. 5. Side view of normally discretized surface line.

One way to improve the surface representation is taking a finer resolution for the discretization, which has the disadvantage that the numerical effort increases. Another way to improve the surface representation is the consideration of skewed surface patches based on the idea of an inclined plane which does not increase the numerical effort considerably. Furthermore, this approach enables the use of the direct transmission of tangential forces over adjacent flanks. Fig. 6 shows the discretized surface line with inclined patches which was originally represented in Fig. 2.

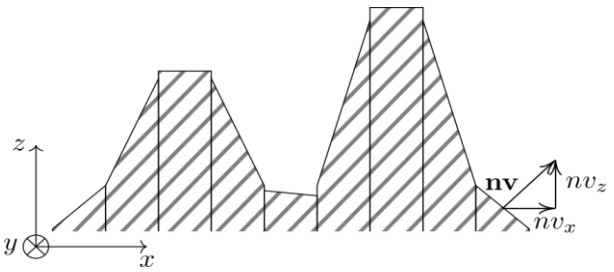

Fig. 6. Side view of discretized surface line with inclined patches.

Each height value h of the discretized surface is the mean value of a subset of s measured points $mp_i = (x_i, y_i, z_i)$. The incline of each surface patch is obtained with a multiple linear regression analysis for each subdivision k with its s elements. In this connection, the regressors α_k, β_k and γ_k describing the inclined plane:

$$z_i = \alpha_k x_i + \beta_k y_i + \gamma_k \tag{19}$$

have to be identified in such a way that the sum of the squared errors between z_i and the target plane is minimized [33]. The least-squares function is:

$$S(\alpha_k, \beta_k, \gamma_k) = \sum_{i=1}^{s} \left[(\alpha_k x_i + \beta_k y_i + \gamma_k) - z_i \right]^2 \tag{20}$$

and its minimization $\nabla S(\alpha_k, \beta_k, \gamma_k) = (0,0,0)$ gives the system:

$$\begin{bmatrix} \sum_{i=1}^{s} x_i^2 & \sum_{i=1}^{s} x_i y_i & \sum_{i=1}^{s} x_i \\ \sum_{i=1}^{s} x_i y_i & \sum_{i=1}^{s} y_i^2 & \sum_{i=1}^{s} y_i \\ \sum_{i=1}^{s} x_i & \sum_{i=1}^{s} y_i & 1 \end{bmatrix} \begin{bmatrix} \alpha_k \\ \beta_k \\ \gamma_k \end{bmatrix} = \begin{bmatrix} \sum_{i=1}^{s} x_i z_i \\ \sum_{i=1}^{s} y_i z_i \\ \sum_{i=1}^{s} z_i \end{bmatrix} \tag{21}$$

The regressors are used to identify the normal vector $\mathbf{nv}_k = (nv_{x,k}, nv_{y,k}, nv_{z,k})$ of each patch. Using the geometry of an inclined plane the '*geometric shear stress*' τ^{geo} caused by the slope of element k in x-direction is derived from the normal vector with:

$$\frac{nv_{x,k}}{nv_{z,k}} = \tan\varphi_k = \frac{\tau_{x,k}^{geo}}{p_k}. \tag{22}$$

The resulting total geometric shear of the whole surface in contact is acquired with the summation over the M elements of the surface which is:

$$\tau^{geo} = \frac{\sum_{k=1}^{M} p_k \cdot \frac{nv_{x,k}}{nv_{z,k}}}{N_x \cdot N_y}, \tag{23}$$

whereat we neglect surface patches with $nv_{x,k} > 0$ as exiting flanks cannot contribute to τ_{geo}. Furthermore, if a patch is deformed solely elastically, the normal vector while in contact is assumed to be the mean of the normal vectors of both contact elements in contact as E and ν of both contact partners are equal for our simulations. If the patch is deformed plastically, the normal vector of the workpiece becomes the

normal vector of the contact patch with which the deformed part is in contact.

Fig. 7 and Fig. 8 show nv_x and nv_y respectively of the DC04 surface and the stamp surface after $p_{mean} = 600$ MPa of Sec. 3.1. They exhibit a uniform distribution in x- and y-direction. Although the contact is severe, the change of nv_x and nv_y is little, but still visible as the amount of surface patches with high nv_x and nv_y decreases.

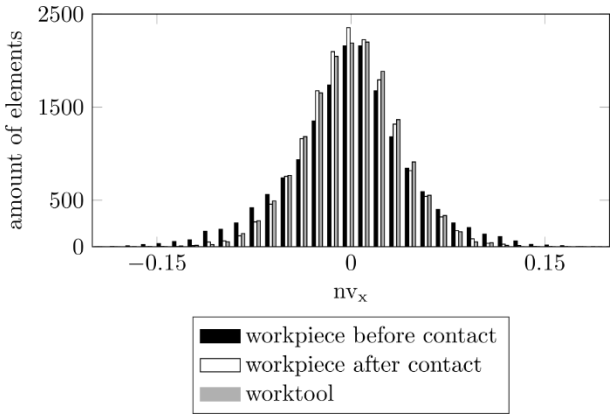

Fig. 7. nv_x of worktool and workpiece before and after contact with p_{mean}=600 MPa.

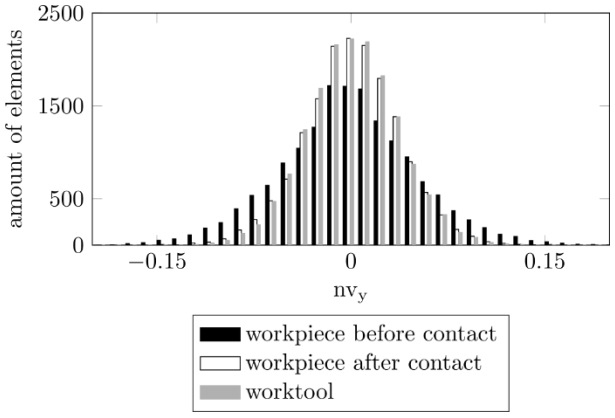

Fig. 8. nv_y of worktool and workpiece before and after contact with p_{mean}=600 MPa

In order to evaluate the impact of the inclined patches on the resulting shear friction, the contact simulation of Sec. 3.1 is extended with the uncoupled tangential contact model of Sec. 2.2. This makes it able to compare τ^{geo} with the adhesive shear stress τ^{adh} which is caused by tangential displacement of both surfaces and transferred by the real contact area A_{real}.

In Fig. 9 the resulting geometric shear stress τ^{geo} and the adhesive shear stress τ^{adh} are depicted over the applied normal load p_{mean}. The symbol $*$ refers to the contact partners from Sec. 3.1. It is evident that τ^{geo} is much lower than τ^{adh} in the whole range of p_{mean}. One reason is the surface roughness of the stamp surface which is much smoother than the DC04 surface. The smooth roughness in turn results in inclined patches which are little deflected from the direction in which the normal contact approach occurs and therefore can contribute only little to τ^{geo}. Hence, a second contact simulation was started which differs from the simulation denoted by $*$ only in a rougher stamp surface with $R_a = 0.240\mu$m and $R_q = 0.303\mu$m. The remaining parameters are not changed. The resulting shear stresses are denoted in Fig. 9 with the symbol ◯. The shear τ^{adh} are for $*$ and ◯ nearly equal, because A_{real} differs in both cases little. In contrast, τ^{geo} shows higher values for ◯ due to the rougher contact partner. Nevertheless, the share of τ^{geo} is still low as it is expected by literature [12].

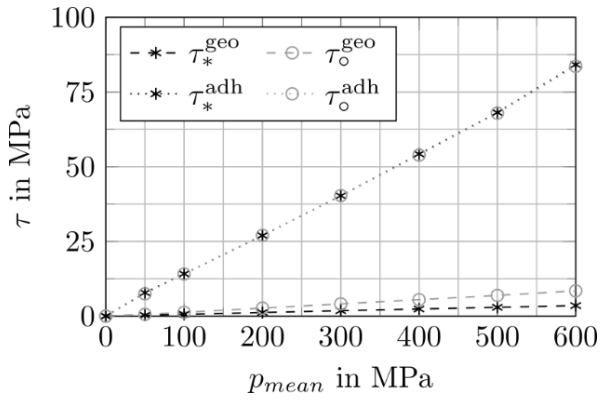

Fig. 9 τ in dependency on p_{mean} for case $*$ and ◯.

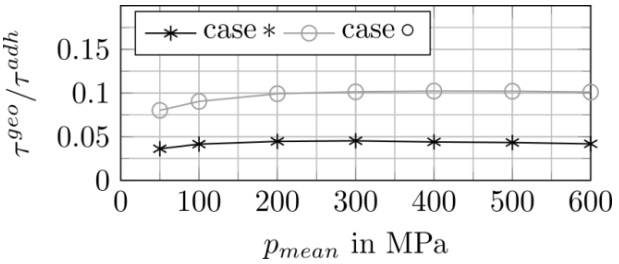

Fig. 10 τ in dependency on p_{mean} for case $*$ and ◯.

Furthermore, the share of τ^{geo} on the total friction resistance is constant in the whole range of p_{mean} which is shown by Fig. 10. Here, the ratio τ^{geo}/τ^{adh} is shown for both $*$ and ◯ which seems to be independent of p_{mean}.

3.1 Work deformation

The next study aims to determine sliding contact of metallic surfaces. Again, the surface of the stamp of Sec. 3.1 is used as elastic contact partner. The discretization parameters remain also. Similar to Sec. 3.1, the elasto-plastic surface is measured from an EDT on a 2mm thick sheet metal made of DC04. This time, the surface of DC04 reaches $L_x \times L_y = 6.33\text{mm} \times 2.11\text{mm}$ and the surface is divided into $N_x \times N_y = 384 \times 128$ elements. The roughness of the DC04 surface changes to $R_a = 0.989\mu\text{m}$ and $R_q = 1.201\mu\text{m}$. The contact between both surfaces is calculated in 257 positions while the elastic contact partner slides in positive x-direction. The normal contact algorithm of Sec. 2.1 is followed by the calculation of the uncoupled tangential contact of Sec. 2.2 for the motion of one element width 2a for each position.

After every shift, a new contact configuration occurs, in which only one element row has not undergone plastic deformation. The work expended for the plastic deformation of the new asperities is interpreted as the dissipated deformation work W^{Def} and its contribution to the frictional resistance is the focus in this section. W^{Def} is equal to the cross-section of the grooved track multiplied by the surface hardness H which is required to plastically displace the peaks of the surface. The contact is simulated for p_{mean} ranging between 100 MPa and 600 MPa in steps of 100 MPa.

Fig. 11 shows the global normal approach u_0 in normal direction over the sliding distance x. In order to attain the desired p_{mean}, the global normal approach has to be adjusted for each contact position. The real contact area A_{real}, which is the ratio of the surface patches in contact to the total surface area, is represented in Fig. 12. Although the ratio increases at first with x, it stagnates very soon.

As A_{real} is responsible for the transferable shear stress, the derived occurring shear work W^{Adh} in each contact position is directly proportional to A_{real} which is shown in Fig. 13.

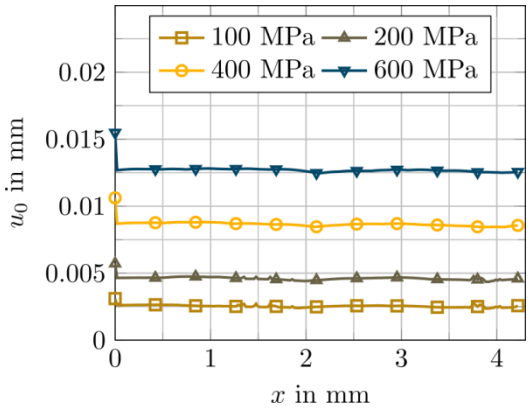

Fig. 11. global approach u_0 in dependency on the tangential displacement x.

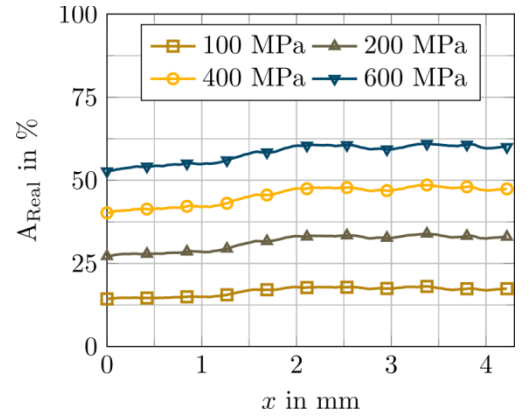

Fig. 12. real contact area A_{real} in dependency on the tangential displacement x.

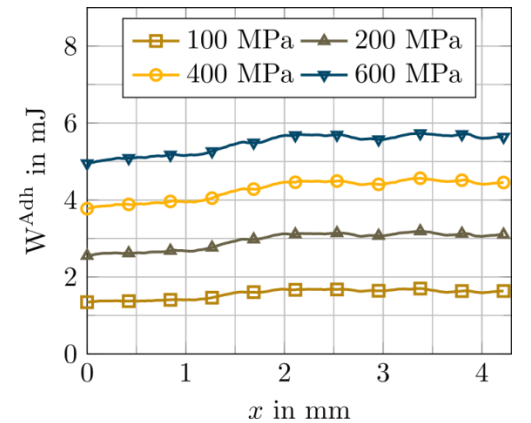

Fig. 13. shear work occurring on each contact postion in dependency on the tangential displacement.

As p_{mean} reaches high values, a huge impact of W^{Def} on the total dissipated frictional work is

assumable due to the severe plastic deformation of the DC04 surface. However, Fig. 14 shows W^{Def} which is dissipated in each contact position and it indicates that the work which is necessary to deform the surface asperities is very low compared to W^{Adh}.

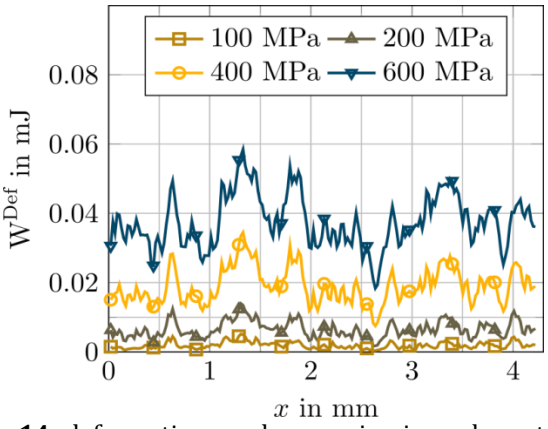

Fig. 14. deformation work occurring in each contact position in dependency on x.

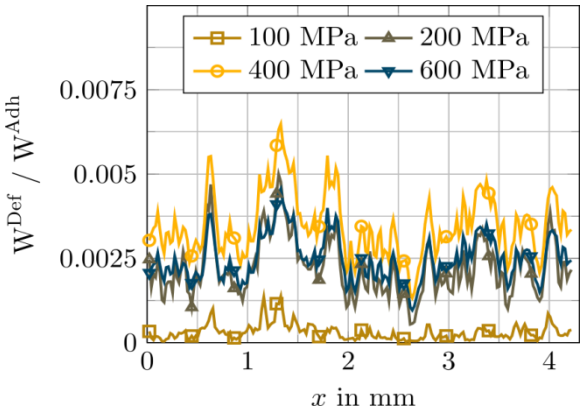

Fig. 15. ratio W^{Def}/W^{Adh} in dependency on the tangential displacement x.

A distinct clarification is given with Fig. 15 in which the ratio W^{Def}/W^{Adh} is shown in dependency on the tangential displacement. As the ratio is in the order of 10^{-3}, the influence of the work needed for the asperity deformation has only a minor impact on the total expended work due to friction.

4. DEDUCTION OF A CONSTITUTIVE FRICTION LAW

In this section a constitutive friction law based on the experiments of section Sec. 3 is presented. It is intended to be applicable for the broad range of normal loads occurring in sheet-bulk metal forming processes.

If two rough surfaces approach, the initial contact is caused by the contact of their asperities. The real contact A_{real} describes the contact of these peaks. A_{real} is smaller than the apparent or global contact area A_0. The ratio A_{real}/A_0 is denoted as α_{rc} in Fig. 16 which is a result of the normal contact simulation of Sec. 3.1. As it can be observed in Fig. 12 and Fig. 13, α_{rc} is an important value, because it is a measure for the transferable shear stress. Hence, the plastic deformation of rough surfaces has a major impact on friction as it changes the ratio in dependency on the applied contact load. α_{rc} increases proportionally with p_{mean} for initial contact which is dominated by plastic deformation.

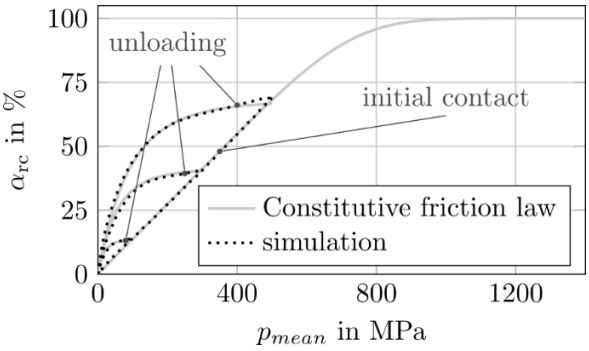

Fig. 16 share of real contact area on apparent area in dependency on contact load.

Although a pressure independent local Tresca law was assumed, the behaviour of α_{rc}, and therewith the behaviour of τ^{adh}, is coinciding with Coulomb's law of friction which is lead back to the linearly rising α_{rc} in dependency on the normal load. The real contact area cannot become higher than the apparent area which is here interpreted as an upper bound for τ_{adh} similar to Tresca's law of friction.

Initial contact is dominated by plastic surface deformation, but re- or unloading the same contact surface multiple times up to the highest experienced normal load is elastic. As the potential contact area is already smoothed for repeated contact, A_{real} is higher compared to initial contact and the average pressure at the same A_{real} is lower. Therefore, the adhesive shear is supposed to be higher for un- or

reloading, as long as the historical highest sustained normal load p_{hist} is not reached. If the contact area is subjected to p_{hist} or higher, the contact becomes elasto-plastic again.

Because of these observations, an alternative constitutive friction law is developed. The initial contact is described similar to Shaw's law of friction [7] and it is defined as:

$$\tau_r = m \cdot \frac{\sigma_y}{2} \cdot \alpha_{rc} = m \cdot \frac{\sigma_y}{2} \cdot \sqrt[n_1]{\tanh\left(\frac{p_{mean} \cdot C_1}{H} \right)^{n_1}} . \qquad (24)$$

It is a local friction law based on Tresca's friction law in the real contact area. As the actual contact area, and therewith α_{rc}, grows with p_{mean} the law shows a linear rise of the transferred shear stress for low to moderate contact loads similar to Coulomb's law of friction. For high contact loads, Eq. (24) becomes constant, because α_{rc} cannot surpass *1*.

The parameters n_1 and C_1 are identified numerically with the half-space model. H is the surface hardness and σ_y is the yield stress of the softer material. The parameter m is Tresca's friction factor which has to be measured anyway, for instance with a ring compression test.

Considering un- and reloading, the friction law is represented by another function as long as p_{mean} is lower than p_{hist}. The modified law is given by

$$\tau_r = m \cdot \frac{\sigma_y}{2} \cdot \sqrt[n_2]{\tanh\left(\frac{p_{mean} \cdot C_2}{H \cdot \alpha_{rc}\left(p_{hist}\right)} \right)^{n_2}} \cdot \alpha_{rc}\left(p_{hist}\right). \qquad (25)$$

It is similar to the initial contact case, where the additional parameters C_2 and n_2 have to be identified. Additionally, the factor $\alpha_{rc}(p_{hist})$, which is the ratio of α_{rc} at the maximum pressure in the previous contacts, is considered to represent the historic sustained contact condition. The results of the half-space model show a high agreement with the constitutive friction law which is shown in Fig. 16.

Sec. 3.2 shows that a worktool surface with low R_a and R_q, which is common for metal forming processes, affects the resulting friction negligible since the ratio τ^{geo} / τ^{adh} is small. Therefore, advancing Eq. (24) and Eq. (25) is not necessary. However, if the worktool surface is rough, which was in the studies $R_a \approx 0.240 \mu m$ and $R_q \approx 0.303 \mu m$ or higher, the impact of the inclined surface patches of the worktool becomes apparent. Although such rough worktool surfaces are uncommon in SBMF, further studies for the advancement of Eq. (24) and Eq. (25) are advisable, as structured worktool surfaces are indeed a matter for SBMF. One plausible assumption is to add a second term to the friction law which gives:

$$\tau_r = m \cdot \left[\frac{\sigma_y}{2} \cdot \alpha_{rc} + f\left(p_{mean}, R_a\right) \right] \qquad (26)$$

for first contact where $f\left(p_{mean}, R_a\right)$ is a function depending on the normal load p_{mean} and the surface roughness R_a.

Furthermore, the results of Sec. 3.3 which focus on the work that is necessary to plastically deform asperities while sliding contact occurs also show that no further change of the friction law is necessary. If two surfaces move tangential to each other new asperities of the undeformed surface get into contact. The work necessary to deform these surface peaks is very low compared to the transferred adhesive work. In fact, the ratio W^{Def} / W^{Adh} shown in Fig. 15 does not surpass *0.008* in any simulation. Therefore, there is no need to consider the friction resistance due to this effect.

5. CONCLUSION

The half-space approximation along with its extensions is a fast and accurate method to determine the elasto-plastic interaction of rough surfaces. Only the two-dimensional surface boundary has to be meshed and solved for the contact problem which comes with a huge advantage compared to the conventional Finite-Element-Method. Although there exist more advanced half-space models that consider three-dimensional plastic deformation, the proposed model is already able to precisely predict the plastic surface deformation by means of roughness parameters. The studies presented here consider different aspects of friction, i.e., normal contact of rough surfaces, inclined

contact elements in the half-space model and sliding contact of rough surfaces. They are combined and evaluated to accurately treat the various contact conditions which arise in sheet-bulk metal forming. The proposed model uses a local friction law of Tresca in the real contact area which adopts Coulomb's friction model for low to moderate contact loads in the whole contact area. The developed friction law consists of two equations. The first one represents the contact conditions at first loading while the second equation takes into account the historic pressure and thus makes it able to change the friction due to the historic elasto-plastic contact. Therefore, it is applicable for un- and reloading. If the worktool surface is rough a second term describing the roughness in dependency on the contact conditions is advisable. However, the study presented here is insufficient for the distinct determination of this term, which in turn can be performed with simulations including worktool surfaces with high R_a and R_q . Nevertheless, since sheet-bulk metal forming processes mostly include wortkools with low R_a and R_q, the constitutive friction law gives an advanced evaluation of the occurring shear stresses due to friction.

Acknowledgement

We gratefully thank the German Research Foundation (DFG) for their support of project C1 of the transregional collaborative research centre (Transregio) 73 that researches the topic of sheet-bulk-metal-forming.

REFERENCES

[1] V.L. Popov, *Contact mechanics and friction: Physical principles and applications*. New York : Springer, 2010.

[2] J.D. Westeneng, 'Modelling of contact and friction in deep drawing processes', *PhD thesis*, University of Twente, Enschede, 2001.

[3] J. Hol, 'Multi-scale friction modeling for sheet metal forming', *PhD thesis*, University of Twente, Enschede, 2013.

[4] F. Zöller, V. Sturm and M. Merklein, 'Experimental and Numerical Investigation on a Pressure Dependent Friction Model', in *16th International Conference on Sheet Metal*, Erlangen, Germany, 2015, pp. 403-411.

[5] M. Merklein, J.M. Allwood, B.-A. Behrens, A. Brosius, H. Hagenah, K. Kuzman, K. Mori, A.E. Tekkaya and A. Weckenmann, 'Bulk forming of sheet metal', *CIRP Annals-Manufacturing Technology*, vol. 61, no. 2, pp. 725-745, 2012.

[6] U. Vierzigmann, J. Koch, M. Merklein and U. Engel, 'Material Flow in Sheet-Bulk Metal Forming', *Key Engineering Materials*, vol. 504-506, pp. 1035-1040, 2012.

[7] M.C. Shaw, 'The role of friction in deformation processing', *Wear*, vol. 6, no. 2, pp. 140-158, 1963.

[8] B.-A. Behrens and A. Sabitovici, 'Modelling of Friction in Deep Drawing considering Irreversible Sheet Surfaces Change', in *Proceedings of the IDDRG 2008 Conference*, Olofström, Sweden, 2008.

[9] J.J. Kalker, *Three-Dimensional Elastic Bodies in Rolling Contact*. Dordrecht: Springer Netherlands, 1990.

[10] J.J. Kalker and Y. van Randen, 'A minimum principle for frictionless elastic contact with application to non-Hertzian half-space contact problems', *Journal of Engineering Mathematics*, vol. 6, no. 2, pp. 193-206, 1972.

[11] H. Hencky, 'Über einige statisch bestimmte Fälle des Gleichgewichts in plastischen Körpern', *ZAMM-Journal of Applied Mathematics and Mechanics*, vol. 3, no. 4, pp. 241-251, 1923.

[12] F.P. Bowden and D. Tabor, *The friction and lubrication of solids*. Oxford and New York: Clarendon Press and Oxford University Press, 1954.

[13] W.T. Kim, B. Bhushan and Y.J. Cho, 'The contact behavior of elastic/plastic non-Gaussian rough surfaces', *Tribology Letters*, vol. 22, no. 1, pp. 1-13, 2006.

[14] X. Tian and B. Bhushan, 'A Numerical Three-Dimensional Model for the Contact of Rough Surfaces by Variational Principle', *Journal of Tribology*, vol. 118, no. 1, p. 33, 1996.

[15] K. Willner, 'Elasto-Plastic Normal Contact of Three-Dimensional Fractal Surfaces Using Halfspace Theory', *Journal of Tribology*, vol. 126, no. 3, pp. 28-33, 2004.

[16] I.A. Polonsky and L.M. Keer, 'A numerical method for solving rough contact problems based on the multi-level multi-summation and conjugate gradient techniques', *Wear*, vol. 231, no. 2, pp. 206-219, 1999.

[17] J.M. Allwood, 'Survey and Performance Assessment of Solution Methods for Elastic

Rough Contact Problems', *Journal of Tribology*, vol. 127, no. 1, p. 10, 2005.

[18] C. Jacq, D. Nelias, G. Lormand and D. Girodin, 'Development of a Three-Dimensional Semi-Analytical Elastic-Plastic Contact Code', *Journal of Tribology*, vol. 124, no. 4, pp. 653-667, 2002.

[19] F. Wang and L.M. Keer, 'Numerical Simulation for Three Dimensional Elastic-Plastic Contact with Hardening Behavior', *Journal of Tribology*, vol. 127, no. 3, pp. 494-502, 2005.

[20] D. Nèlias, V. Boucly and M. Brunet, 'Elastic-Plastic Contact Between Rough Surfaces: Proposal for a Wear or Running-in Model', *Journal of Tribology*, vol. 128, no. 2, p. 236, 2006.

[21] J.J. Kalker, 'The computation of three-dimensional rolling contact with dry friction', *International Journal for Numerical Methods in Engineering*, vol. 14, no. 9, pp. 1293-1307, 1979.

[22] K. Vàradi, Z. Néder and K. Friedrich, 'Evaluation of the real contact areas, pressure distributions and contact temperatures during sliding contact between real metal surfaces', *Wear*, vol. 200, no. 1-2, pp. 55-62, 1996.

[23] K. Willner, 'Fully Coupled Frictional Contact Using Elastic Halfspace Theory', *Journal of Tribology*, vol. 130, no. 3, p. 031405, 2008.

[24] W.W. Chen and Q.J. Wang, 'A Numerical Static Friction Model for Spherical Contacts of Rough Surfaces, Influence of Load, Material, and Roughness', *Journal of Tribology*, vol. 131, no. 2, p. 021402, 2009.

[25] B. Fulleringer, D. Nèlias: *On the Tangential Displacement of a Surface Point Due to a Cuboid of uniform Plastic Strain in a Half-Space*, Journal of Applied Mechanics, Vol. 77, p. 021014, 2010.

[26] V. Boucly, D. Nèlias and I. Green, 'Modeling of the Rolling and Sliding Contact Between Two Asperities', *Journal of Tribology*, vol. 129, no. 2, p. 235, 2007.

[27] J. Boussinesq, *Applications des potentiels à l'étude de l'équilibre et du mouvement des solides èlastiques*. Gauthier-Villars, 1885.

[28] K.L. Johnson: *Contact Mechanics*. Cambridge: Cambridge University Press, 1985.

[29] A.E. Love, 'The Stress Produced in a Semi-Infinite Solid by Pressure on Part of the Boundary', *Philosophical Transactions of the Royal Society A: Mathematical, Physical and Engineering Sciences*, vol. 228, no. 659-669, pp. 377-420, 1929.

[30] F. Hauer, 'Die elasto-plastische Einglättung rauer Oberflächen und ihr Einfluss auf die Reibung in der Umformtechnik', *PhD thesis*, Chair of Applied Mechanics, Friedrich-Alexander-Universität Erlangen-Nürnberg, Erlangen, 2014.

[31] J. Pullen and J.B. Williamson, 'On the Plastic Contact of Rough Surfaces', *Proceedings of the Royal Society A: Mathematical, Physical and Engineering Sciences*, vol. 327, no. 1569, pp. 159-173, 1972.

[32] V. Cerruti, *Ricerche intorno all'equilibrio de'corpi elastici isotropi: Memoria del Valentino Cerruti.* Rome: Salviucci, 1882.

[33] D.C. Montgomery, E.A. Peck and G.G. Vining: *Introduction to linear regression analysis*. Hoboken: Wiley, 2012.

Nomenclature

α , β , γ	regressors for multiple linear regression
α_{rc}	ratio of real contact area to apparent contact area
(x, y)	arbitrary surface point
(x', y')	surface point subjected to contact load
ν_1 and ν_2	Poisson's ratio of two contact bodies
Ω	contact domain
σ_y	yield stress
τ^{adh}	adhesive shear stress caused by tangential displacement of contacting surfaces
τ^{geo}	geometric shear stress caused by inclined surface patches
$\mathbf{nv} = (nv_x, nv_y, nv_z)$	normal vector which defines a contact element of the contact surface
a and b	half length of a contact element in x-direction and y-direction
A_{real} and A_0	real contact area and apparent contact area
C	influence coefficient matrix
E_1 and E_2	Young's moduli of two contact bodies
E^* and E'	composite elastic moduli
H	surface hardness
h	local height coordinate
h_{max}	maximum surface coordinate
k	index of surface element
l	index of surface elements that are in contact
L_x and L_y	length of discretized surface

	in x- and y-direction
M	total number of contact elements
mp	concrete height points which a in a subset
N_x and N_y	number of contact elements in x- and y-direction
p , q_x and q_y	local contact pressure and shear tractions
p_{mean}	average contact load at whole surface
R_a	centre-line surface average
R_q	root mean square roughness
S	least-squares function
s	number of measured points in a subset which is used to

	discretize a surface element
u^{el}	elastic surface displacement
u^{pl}	plastic surface displacement
u_0	global normal approach in z-direction
u_x , u_y and u_z	surface displacements
W^{Adh}	dissipated work due to tangential displacement of contacting surfaces
W^{Def}	dissipated work due to plastic deformation of surface asperities
x , y , z	space coordinates